Biomechanics and Modeling in Mechanobiology (2021) 20:1561–1578
https://doi.org/10.1007/s10237-021-01463-3

ORIGINAL PAPER

# Multi-physics modeling and finite element formulation of corneal UV cross-linking

**Shuolun Wang**[1] · **Shawn A. Chester**[2]

Received: 14 November 2020 / Accepted: 3 May 2021 / Published online: 19 May 2021


**Abstract**
The UV cross-linking technique applied to the cornea is a popular and effective therapy for eye diseases such as keratoconus and ectatic disorders. The treatment strengthens the cornea by forming new cross-links via photochemical reactions and, in turn, prevents the disease from further developing. To better understand and capture the underlying mechanisms, we develop a multi-physics model that considers the migration of the riboflavin (i.e., the photo-initializer), UV light absorption, the photochemical reaction that forms the cross-links, and biomechanical changes caused by changes to the microstructure. Our model is calibrated to a set of nanoindentation tests on UV cross-linked corneas from the literature. Additionally, we implement our multi-physics model numerically into a commercial finite element software. We also compare our simulation against a set of inflation tests from the literature. The simulation capability allows us to make quantitative predictions of a therapy's outcomes in full 3-D, based on the actual corneal geometry; it also helps medical practitioners with surgical planning.

**Keywords** UV cross-linking · Biological material · Multi-field problems · Finite elements

## 1 Introduction

Keratoconus is a noninflammatory conelike ectasia of the cornea (Rad et al. 2004). It is a result of progressive corneal disease or a sequela of refractive surgery (Dahl et al. 2012). The reported average frequency of such disease in the human population is around 1 per 2000 to 1 per 500 (Rabinowitz 1998). Wearing hard contact lenses are considered to be the conventional treatment (Dana et al. 1992). The severe cases have to be treated with invasive operations such as penetrating keratoplasty, epikeratoplasty, photorefractive keratectomy (Jaeger et al. 1987; Sekundo and Stevens 2001). Nevertheless, none of those treatments can stop the disease from further developing; instead, they only act to correct the refractive errors. On the other hand, the cross-linking technique is based on the photo-polymerization of the collagen fibrils within the cornea, which has become popular recently. It stabilizes or even halts the disease's progression by forming new cross-links to strengthen the collagen fibrils. As evidenced by mechanical testing, the technique improves the cornea's stiffness and biomechanical properties (Spoerl et al. 1998; Wollensak et al. 2003; Kling et al. 2010; Seifert et al. 2014).

Cross-linking, as a method to stiffen materials in a biomedical setting, is not a new concept. In various medical fields, dentists have long utilized UV light to harden the filling resins through photochemical reactions (Lovell et al. 2001), and prosthetic heart valves have been strengthened through the cross-linking process with glutaraldehyde (Golomb et al. 1987) for decades. In industrial settings, UV light is in widespread use to harden adhesives (Goss 2002). Furthermore, in the realm of 3-D printing, complex parts have been manufactured precisely and rapidly via photo-polymerization (Maruo et al. 1997; Han et al. 2019) for a long time as well.

The idea of corneal UV cross-linking treatment emerges when much work has recently been done on identifying the biological glues that could strengthen collagen fibrils within the cornea (Mazzotta et al. 2007). Researchers noticed that diabetic patients seldom develop keratoconus due to the glycosylation-mediated cross-linking (Seiler et al. 2000; Kuo et al. 2006). Inspired by this finding, a standard protocol (the so-called Dresden protocol) of corneal UV cross-linking was

✉ Shuolun Wang
swang25@nd.edu

[1] Department of Aerospace and Mechanical Engineering, University of Notre Dame, Notre Dame, IN 46556, USA

[2] Mechanical Engineering, New Jersey Institute of Technology, Newark, NJ 07102, USA

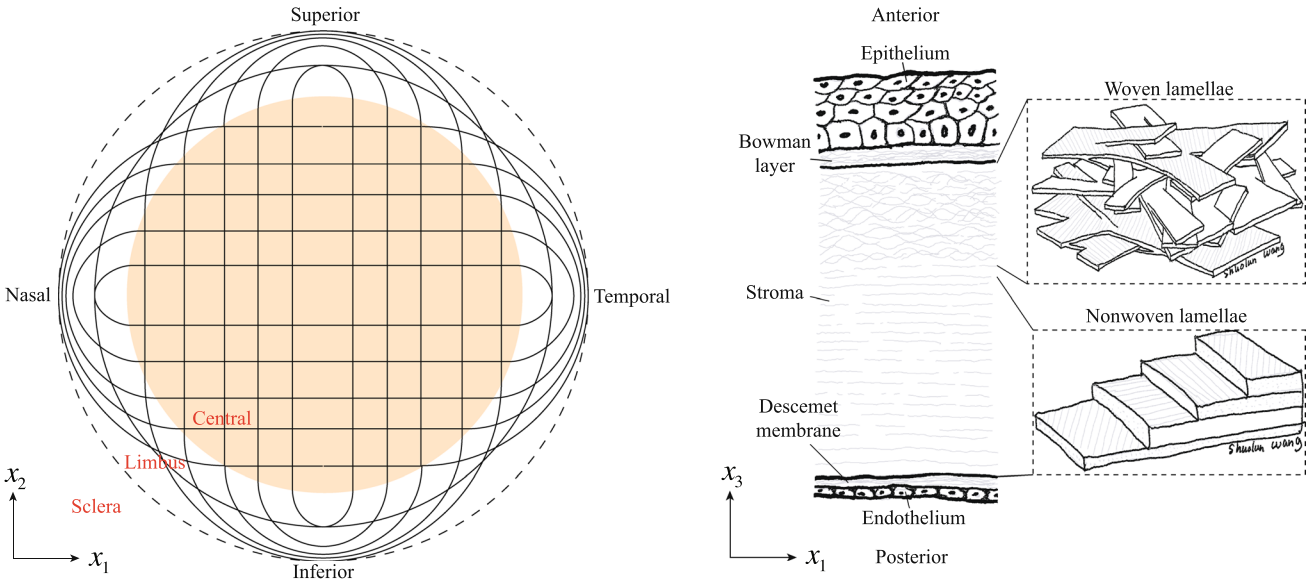


**Fig. 1** Schematic of a typical human cornea, showing key regions, mean collagen fibril orientations, and microstructures. Left: the top view based on a previous work (Pandolfi and Holzapfel 2008). The key components are Central—a circular region with a radius about 4.5 mm; Limbus—a ring border about 1.5 to 2 mm wide that encircles the periphery of the central region; Sclera—the opaque tissue of the eye; Nasal—the side near the nose; Inferior—the south side; Temporal—the opposite side of nasal; Superior—the north side; Anterior—the outer surface; Posterior—the innermost surface. Right: the side view with various anatomic layers along with the thickness. The magnified views demonstrate the lamellae's microstructures within the stroma, where lamellae are highly interweaving near the anterior side and parallel near the posterior side

established based on the initial work by Spoerl et al. (2007). The protocol consists of two steps: The first step involves the de-epithelization within a diameter of 8–10 mm, followed by saturation of riboflavin solution (i.e., a photo-initiator) with a concentration of 0.1%. Note that a 30 minutes dwell time is expected to ensure a desired distribution of the riboflavin. During the second step, the anterior surface (see Fig. 1) is irradiated with UV light with a 365 nm wavelength for 30 minutes with radiation intensity of 3 mW/cm$^2$, which corresponds to an energy dose of 5.4 J/cm$^2$. Meanwhile, the riboflavin is fed dropwise onto the anterior surface every 5 min to maintain its abundance. Besides the standard protocol, many additional efforts have been made to accelerate the treatment (Schumacher et al. 2011; Wernli et al. 2013; Beshtawi et al. 2013), but are not described in detail here.

Optimization of the treatment requires a comprehensive understanding of the underlying mechanisms governing the entire process. The essential mechanisms related to this process's fundamental kinetics are not yet agreed upon and limited to about ten published articles by a small group of researchers (Kamaev et al. 2012; Schumacher et al. 2012; Goh et al. 2014; Semchishen et al. 2015; Caruso et al. 2017; Kling and Hafezi 2017; Lin 2016, 2018). The common understanding is that riboflavin serves as a primary acceptor of the UV radiation, capable of migrating into the tissue through diffusion. Once exposed to the UV light, it absorbs the UV energy and is excited to its triplet state. There are two pathways for the photochemical reaction depending on the oxygen level available within the tissue. In the type-I reaction, the excited triplet state reacts directly with the collagen fibrils creating free radicals that cause hydrogen bonds or cross-link formation between the amino acids on the collagen fibrils at the intra and interhelical levels as well as the intermicrofibrillar level. In the type-II reaction, the excited riboflavin reacts with oxygen to form reactive singlet oxygen, further reacting with the collagen covalent bonds between the collagen molecules to produce additional cross-links. Under typical ambient conditions, the type-I reaction dominates the process because the type-II reaction consumes oxygen too rapidly from the environment. In addition to corneal UV crosslinking, Goh et al. (2014) proposed a general thermomechanical framework/road map of modeling the outcomes brought by UV crosslinking on various biological tissues. In their work, they considered the mechanics of UV-tissue interaction, biomechanical response, and photo-initializer effects.

To the best of our knowledge, most existing corneal UV treatment models are limited to only 1-D and are solved analytically or via a finite difference method. However, such simplifications fail to take practical considerations into accounts, such as the actual cornea state and geometry. For example, keratoconus is generally localized; the treatments' efficacy could be improved by stiffening only the weakened parts of the cornea (Singh et al. 2017). Additionally,

customizable surgical planning would be possible and beneficial to patients when considering actual geometries from individuals. Thus, the formulation of a 3-D photo-chemical-mechanically coupled finite element implementation to simulate the corneal UV treatment on actual corneal geometry is required for personalized treatment or process improvement.

This work's main objective is to formulate a multi-physics model and verifies a finite element implementation that can reliably and robustly solve arbitrary 3-D photo-chemical-mechanically coupled boundary value problems applied to corneal UV treatment. Specifically, we focus our attention on corneal UV cross-linking treatment that involves diffusion of riboflavin, UV light absorption, photochemical reactions, and finite deformation biomechanics. Our model is calibrated against a set of nanoindentations tests by Seifert et al. (2014), and the finite element implementation is based on a user-defined element (UEL) in commercial software packages Abaqus/Standard (2019). The simulations with actual corneal geometry are compared against the inflation tests reported by Kling et al. (2010).

The remainder of the paper is organized as follows. In Sect. 2, we present our mathematical model. Section 3 demonstrates the results and the comparison between our simulations and the experiments. Section 4 summarizes the paper, followed by possible future improvements. In the Appendix, we cover the details of finite element implementation, the tangents needed for the iterative solver, verifications of the numerical implementation, and a sensitivity study.

## 2 Method

The UV cross-linking is a rather complicated process that involves: (1) radiative transfer, (2) migration of riboflavin (photo-initiator), (3) photochemical reaction, and (4) biomechanics. We will elaborate on each phenomenon, their coupling, and our continuum-based mathematical model in this section.

### 2.1 Kinematics

The notation we use follows standard continuum mechanics (Gurtin et al. 2010).[1] We let $\mathcal{B}_{\mathrm{R}}$ denote a continuous region of space that the cornea occupies in a fixed reference configuration, and a material point is denoted by $\mathbf{x}_{\mathrm{R}}$. $\mathcal{B}_t$ denotes a region that material body occupies in the current state, and a spatial point in this region is denoted as $\mathbf{x}$. We define the motion $\chi$ which maps the material points from the reference body to the current body

$$\mathbf{x} = \chi(\mathbf{x}_{\mathrm{R}}, t) \tag{2.1}$$

The deformation gradient, Jacobian, and the left and right Cauchy-Green tensors are given by

$$\mathbf{F} = \nabla\chi, \quad J = \det\mathbf{F} > 0, \quad \mathbf{B} = \mathbf{F}\mathbf{F}^{\mathsf{T}}, \quad \mathbf{C} = \mathbf{F}^{\mathsf{T}}\mathbf{F}. \tag{2.2}$$

*Importantly*, we note that during the UV treatment, the entire cornea is held fixed in the reference state, and the new crosslinks are formed stress-free in the referential configuration $\mathcal{B}_{\mathrm{R}}$.

### 2.2 Radiative transfer

Radiative transfer is required since the literature shows that the UV light undergoes apparent absorption within the cornea (Wollensak et al. 2003). Accordingly, we must model the intensity of the UV light through the thickness of the cornea. Following Chandrasekhar (2013), the governing equation for radiative transfer is given by

$$\frac{1}{v_c}\frac{\partial I}{\partial t} + d\cdot\mathrm{grad}I + (k_a + k_s)I = j + \frac{1}{4\pi v_c}k_s\int_{\mathcal{B}_t} I\mathrm{d}v, \tag{2.3}$$

where $v_c$ is the speed of light, $\mathbf{d}$ is the direction of the light propagation, $I$ is the light intensity, $k_a$ is the absorption coefficient, $k_s$ is the scattering coefficient, and $j$ is the emission. The last term in Eq. (2.3) is the integral of scattered light over the entire body $\mathcal{B}_t$.

Next, we only consider monochromatic light and assume that the speed of light is significantly larger than the time scale of the other phenomenon we wish to model. We also ignore all the possible scattering and emission. With assumptions, the simplified form of Eq. (2.3) is reduced to the well known Beer-Lambert law (Swinehart 1962)

$$\mathbf{d}\cdot\mathrm{grad}I + \sigma I = 0, \tag{2.4}$$

where $\sigma(\mathbf{x}, t)$ denotes the extinction field, which takes into account attenuation of the light through the material in a lumped manner. More specifically, we assume the extinction field is given by

$$\sigma(\mathbf{x}, t) = \epsilon_{\mathrm{r}} c_{\mathrm{R}} + \sigma_{\mathrm{c}}, \tag{2.5}$$

where $\epsilon_{\mathrm{r}}$ is the absorption coefficient of riboflavin, $c_{\mathrm{R}}(\mathbf{x}, t)$ is the photo-initiator's concentration per reference volume, and $\sigma_{\mathrm{c}}$ takes into account light absorption by the cornea itself.

### 2.3 Migration of riboflavin

The migration of the riboflavin is governed by a diffusion-reaction equation

[1] The symbols $\nabla$ and Div denote the gradient and divergence with respect to the material point $\mathbf{x}_{\mathrm{R}}$ in the reference configuration, while grad and div denote these operators with respect to the point $\mathbf{x} = \chi(\mathbf{x}_{\mathrm{R}}, t)$ in the deformed configuration.

$$\dot{c}_{\mathrm{R}} = -J\mathrm{div}(\mathbf{j}) - JR_{\mathrm{c}}, \tag{2.6}$$

where $\mathbf{j}$ denotes the flux of riboflavin that we assume follows Fick's first law

$$\mathbf{j} = -\mathbf{D}\mathrm{grad}c_{\mathrm{R}}. \tag{2.7}$$

As an approximation, the diffusion is assumed to be isotropic, making the diffusivity tensor $\mathbf{D}$ in Eq. (2.7) reduce to $D\mathbf{1}$, with $D$ a scalar diffusivity. Next, the reaction term $R_{\mathrm{c}}$ in Eq. (2.6) denotes the depletion rate of the riboflavin. Regarding to the experiments by Ahmad et al. (2004), the consumption of riboflavin is barely noticeable even with intensive UV light of 30 mW/cm$^2$ for quite long time, accordingly we assume $R_{\mathrm{c}} = 0$ as is the case for most of the literature (Schumacher et al. 2012; Kamaev et al. 2012; Kling and Hafezi 2017).

### 2.4 Photochemical reaction

We follow the chemistry literature (Odian et al. 2004; Watts 2005), in which the UV cross-linking process is modeled as a polymerization reaction consisting of three phases: (1) initiation, (2) propagation, and (3) termination. Initiation creates free chain radicals, whose concentration per unit reference volume is denoted by $[M_*]$, which are necessary for propagation. In particular, the free radicals are created from the photoinitiator riboflavin under UV exposure with a rate of $R_{\mathrm{i}}$. Next, propagation is the rapid reaction of radicalized molecules with the monomer, with concentration per unit reference volume denoted by $[M]$, with a rate of $R_{\mathrm{p}}$. Moreover, the propagation reaction happens repetitiously to form long polymeric chains and cross-links. Lastly, the termination reaction occurs when two free chain radicals react to form a single molecule with a rate of $R_{\mathrm{t}}$.

The rate of monomer disappearance is equivalent to the rate of polymerization (Watts 2005),

$$-[\dot{M}] = R_{\mathrm{i}} + R_{\mathrm{p}} + R_{\mathrm{t}}, \tag{2.8}$$

which is the sum of rates of initiation $R_{\mathrm{i}}$, propagation $R_{\mathrm{p}}$, and termination $R_{\mathrm{t}}$. It is assumed that the rate of propagation is significantly larger than other rates (i.e., $R_{\mathrm{p}} \gg R_{\mathrm{i}}, R_{\mathrm{p}} \gg R_{\mathrm{t}}$), thus as a first order approximation (Watts 2005; Schumacher et al. 2012), Eq. (2.8) is approximated by

$$-[\dot{M}] \approx R_{\mathrm{p}} = k_{\mathrm{p}}[M_*][M], \tag{2.9}$$

where $k_{\mathrm{p}}$ is the rate constant for the propagation reaction. At steady state, the concentration of free chain radicals attains a constant value, and then it is equivalent to saying that the rate of initiation and termination are equal (Watts 2005),

$$R_{\mathrm{i}} = R_{\mathrm{t}} = 2k_{\mathrm{t}}[M_*]^2, \tag{2.10}$$

where $k_{\mathrm{t}}$ is the rate constant for the termination reaction. Using Eqs. (2.10) in (2.9), at steady state the rate of monomer disappearance becomes

$$-[\dot{M}] \approx R_{\mathrm{p}} = k_{\mathrm{p}}[M]\sqrt{\frac{R_{\mathrm{i}}}{2k_{\mathrm{t}}}}. \tag{2.11}$$

Next, based on Watts (2005), the rate of initiation is given by

$$R_{\mathrm{i}} = 2\Phi I_a \quad \text{with} \quad I_a = \epsilon_{\mathrm{r}} c_{\mathrm{R}} I, \tag{2.12}$$

where $\Phi$ denotes the quantum yield for the chemical initiation, $I_{\mathrm{a}}$ indicates the amount of light absorbed by riboflavin per unit volume. The factor of 2 appearing in Eq. (2.12) indicates two free chain radicals generated for each riboflavin molecule. Finally, with Eq. (2.12) inserted into Eq. (2.11), the final expression for the steady state polymerization rate is written in the form

$$-[\dot{M}] \approx k_{\mathrm{p}}[M]\sqrt{\frac{\Phi\epsilon_{\mathrm{r}} c_{\mathrm{R}} I}{k_{\mathrm{t}}}}. \tag{2.13}$$

Unlike the previous work of Goh et al. (2014), in which they modeled the rate of accumulation of UV-induced cross-links as a nonlinear function based on a logistic approach (Sadkowski 2000), the derivation here produces a linear differential equation for the photochemical reaction. To keep track of the status of the photochemical reaction, we use a scalar measure—the degree of cross-linking—defined by

$$\xi = \frac{[M_0] - [M]}{[M_0]}, \tag{2.14}$$

where $[M_0]$ denotes the initial concentration of monomer per reference volume.

### 2.5 Biomechanics

The cornea consists of an incompressible extracellular matrix and $\alpha = 1, 2, \ldots, N$ families of dispersively oriented collagen fibrils with the unit vector $\mathbf{a}_0^{(\alpha)}$ denoted as their mean orientation in the reference state (Gasser et al. 2006; Pandolfi and Holzapfel 2008; Wang and Hatami-Marbini 2021). We use invariant $I_{\mathrm{f}}^{(\alpha)}$ to measure the physical stretching of each family of the collagen fibrils

$$I_{\mathrm{f}}^{(\alpha)} = \mathrm{tr}(\mathbf{H}^{(\alpha)}\mathbf{C}), \tag{2.15}$$

where $\mathbf{H}^{(\alpha)}$ is the generalized structure tensor measuring the degree of dispersion of collagen fibrils (Gasser et al. 2006)

$$\mathbf{H}^{(\alpha)} = \kappa^{(\alpha)}\mathbf{1} + (1 - 3\kappa^{(\alpha)})\mathbf{a}_0^{(\alpha)} \otimes \mathbf{a}_0^{(\alpha)} \tag{2.16}$$

with $0 \le \kappa^{(\alpha)} \le 1/3$ the dispersion parameter. Note the case of perfect alignment is achieved when $\kappa^{(\alpha)} = 0$, while the

case of a pure isotropic distribution is reproduced when $\kappa^{(\alpha)} = 1/3$.

The total Cauchy stress is given by a contribution due to the extracellular matrix and a contribution due to each of the collagen fibril families (Pandolfi and Holzapfel 2008; Wang and Hatami-Marbini 2021),

$$\mathbf{T} = \mathbf{T}^{\mathrm{m}} + \sum_{\alpha=1}^{N} \mathbf{T}^{\mathrm{f}(\alpha)}. \tag{2.17}$$

The extracellular matrix is modeled as an incompressible neo-Hookean material (Pandolfi and Holzapfel 2008; Wang and Hatami-Marbini 2021),

$$\mathbf{T}^{\mathrm{m}} = G\mathbf{B} + P\mathbf{1}\,, \tag{2.18}$$

where $G$ and $P$ denote the shear modulus and an undetermined pressure, respectively. Next, the collagen fibrils in the cornea are found to exhibit stretch locking behavior (Pandolfi and Holzapfel 2008), thus we model them using an exponential form (Pandolfi and Holzapfel 2008; Petsche and Pinsky 2013; Wang and Hatami-Marbini 2021),

$$\mathbf{T}^{\mathrm{f}(\alpha)} = \left[k_1\left(I_{\mathrm{f}}^{(\alpha)} - 1\right)\exp\left(k_2\left(I_{\mathrm{f}}^{(\alpha)} - 1\right)^2\right)\right]\mathbf{F}\mathbf{H}^{(\alpha)}\mathbf{F}^T, \tag{2.19}$$

where $k_1$ and $k_2$ are initial and locking fiber modulus, respectively. It is also worth noting that the collagen fibrils are *not* able to withstand any compression, so if $I_{\mathrm{f}}^{(\alpha)} \leq 1$, the fiber stress is omitted in (2.17).

As noted in the recent study by Germann et al. (2020), the cross-links are formed between collagen fibrils and other macromolecules in the cornea. And the overall macroscopic effect is an increased elastic modulus and stretch locking behavior, as seen in experiments (Kling et al. 2010; Seifert et al. 2014). Accordingly, we model this increase in the number of cross-links as a modification to all factors that contribute to the material's mechanical behavior. Specifically, we let the shear modulus in Eq. (2.18) and initial and locking fiber modulus in Eq. (2.19) depend linearly on the degree of cross-linking $\xi$,

$$G(\xi) = G_0 + \xi G_1, \quad k_1(\xi) = k_{10} + \xi k_{11}, \quad \text{and} \quad k_2(\xi) = k_{20} + \xi k_{21}, \tag{2.20}$$

where $\{G_0, k_{10}, k_{20}\}$ are initial parameters before the treatment ($\xi = 0$), while $\{G_1, k_{11}, k_{21}\}$ are the parameters when fully cross-linked ($\xi = 1$).

Overall, the evolution of mechanical properties with the UV irradiation time in this work is different from Goh et al. (2014). When given the same photochemical condition and compared at the same material point, the mechanical properties in this work increase with the UV irradiation time according to an exponential saturation function. Simultaneously, the shear modulus in Goh et al. (2014) is a sigmoid function of UV irradiation time.

### 2.6 Governing equations

The summary of the coupled partial differential equations is:

- Radiative transfer

$$\begin{cases} \mathbf{d}\cdot\mathrm{grad}I + \sigma I = 0 & \text{in} \quad \mathcal{B}_t, \\ I = I_0 & \text{on} \quad \mathcal{S}_I, \end{cases} \tag{2.21}$$

  where $\mathcal{S}_I$ is the portion of the boundary that UV light with an intensity of $I_0$ irradiated onto it.
- Conservation of riboflavin

$$\begin{cases} \dot{c}_{\mathrm{R}} - \mathrm{div}(D\mathrm{grad}c_{\mathrm{R}}) = 0 & \text{in} \quad \mathcal{B}_t, \\ c_{\mathrm{R}} = c_0 & \text{on} \quad \mathcal{S}_c, \\ -\mathbf{j}\cdot\mathbf{n} = \breve{j} & \text{on} \quad \mathcal{S}_{\mathbf{j}}, \end{cases} \tag{2.22}$$

  where $\mathcal{S}_c$ is the portion of the boundary where the concentration of riboflavin $c_0$ is prescribed, and $\mathcal{S}_{\mathbf{j}}$ is the portion of the boundary surface with outward normal $\mathbf{n}$ prescribed with flux $\breve{j}$.
- Balance of linear momentum

$$\begin{cases} \mathrm{div}\mathbf{T} = \mathbf{0} & \text{in} \quad \mathcal{B}_t, \\ \mathbf{u} = \breve{\mathbf{u}} & \text{on} \quad \mathcal{B}_{\mathbf{u}}, \\ \mathbf{T}\mathbf{n} = \breve{\mathbf{t}} & \text{on} \quad \mathcal{S}_{\mathbf{t}}, \end{cases} \tag{2.23}$$

  where $\mathcal{B}_{\mathbf{u}}$ is the portion of the boundary with the prescribed displacement $\breve{\mathbf{u}}$, and $\mathcal{S}_{\mathbf{t}}$ is the portion of the boundary prescribed with the traction $\breve{\mathbf{t}}$.

At this point, the coupling between UV irradiation and photochemistry becomes clear. As mentioned in the discussion related to Eq. (2.5), the extinction field $\sigma$ consists of cornea's absorption $\sigma_{\mathrm{c}}$ and concentration-dependent portion $\epsilon_{\mathrm{r}}c_{\mathrm{R}}$. The latter links two physical fields in the "one way" manner—the distribution of riboflavin's concentration affects the UV light intensity field, but the UV light intensity does not affect the concentration of riboflavin, in this particular case. More importantly, the concentration of monomer per reference volume $[M]$ or the degree of cross-linking $\xi$ is the essential coupling between photochemistry and biomechanics. We save both $[M]$ and $\xi$ as state-variables locally at each material point and update them according to Eqs. (2.13) and (2.14).

We solve the coupled boundary value problem consisting of Eqs. (2.21), (2.22), and (2.23) numerically via the finite element method. Following our previous work (Chester et al. 2015; Wang et al. 2016; Hamel et al. 2017; Bosnjak et al. 2019), our model is implemented in Abaqus/Standard (2019) by writing user-defined element subroutines (UEL).

The details of numerical implementation are presented in Appendix 1. Also, we have verified the numerical implementation by comparing numerical solutions against analytically tractable solutions in Appendix 2. And lastly, a sensitivity study of our model by varying material parameters and boundary conditions is presented in Appendix 3.

## 3 Results and discussion

In this section, we calibrate our model to both nanoindentation tests (Seifert et al. 2014) and inflation tests (Kling et al. 2010) on porcine cornea from the literature. We adopt this two-stage approach since we are unaware of a single experimental data set that is comprehensive, including all portions from photochemical reaction rates to large deformation biomechanics. Our calibration is based on the following observations of the experimental data:

- The nanoindentation experiments performed by Seifert et al. (2014) contain detailed photochemical information, but do not have adequate large deformation biomechanics. Figure 4 shows the measured profile of Young's modulus across the thickness for UV-treated corneal samples and control samples.
- The inflation experiments performed by Kling et al. (2010) are lacking photochemical information, but are rich in large deformation biomechanics. Figure 6d shows the measured apical displacement-intraocular pressure (IOP) curves for UV-treated corneal samples and control samples.

Accordingly, our procedure will exploit the fact that these two data sets together contain all the information our model requires. We first consider the nanoindentation tests by Seifert et al. (2014) and then focus attention on the inflation experiments of Kling et al. (2010).

### 3.1 Simulation of nanoindentation tests from the literature

*Finite element mesh and boundary conditions* In our simulation, we consider a slender 3-D block with a dimension of $w \times w \times l = 250\,\mu\text{m} \times 250\,\mu\text{m} \times 800\,\mu\text{m}$, see Fig. 2. The entire domain is discretized into 4500 8-node brick elements. We treat the photochemical reaction across the corneal thickness (in $x_1$ direction) as a 1-D problem, which is in line with the experiments by Seifert et al. (2014). The corneal samples in the experiments were taken from the central region (see Fig. 1), where both UV light intensity and concentration of the riboflavin are at the highest level, making the photochemical reaction dominant in the thickness direction. Note that we place nine spherical indenters with

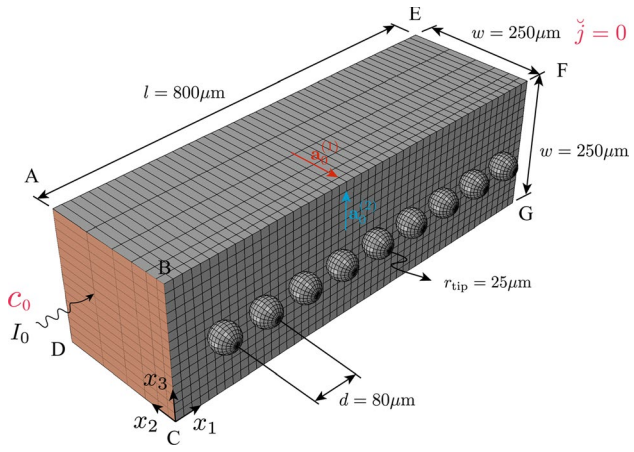


**Fig. 2** Geometry, finite-element mesh, and boundary conditions used in the indentation simulations. Nine spherical indenters are equally-spaced across the corneal thickness. Two families of collagen fibrils are denoted as referential unit vectors $\mathbf{a}_0^{(1)}$ and $\mathbf{a}_0^{(2)}$, respectively

the radius of $r_{\text{tip}} = 25\,\mu$m for the indentation. All indenters are equally-spaced across the corneal thickness leading to a spacing of $d = 80\,\mu$m.

Our simulation strictly follows the standard protocol used in the experiment, which consists of the intake of the riboflavin solution for the first half-hour, followed by UV irradiation at the anterior side for the second half-hour without any deformation. After the UV cross-linking, each of the nine indenters loads then unloads in the $x_2$ direction, with the reaction force being recorded.

For the initial conditions, we assume no riboflavin, and a stress-free undeformed body, in the entire domain at $t = 0$. Referring to Fig. 2, for the photochemical boundary conditions, we prescribe the riboflavin with a concentration of $c_0 = 0.1\%$ and a UV light with an intensity of $I_0 = 3$ mW/cm$^2$ on face ABCD ($x_1 = 0$, anterior side), and no flux condition $\check{j} = 0$ on face EFGH ($x_1 = 800\,\mu$m, posterior side). We assume that the UV light propagates in $x_1$ direction ($\mathbf{d} = \mathbf{e}_1$). Figure 3a shows the photochemical boundary conditions as a function of time at $x_1 = 0$. Again, referring to Fig. 2, when it comes to the mechanical boundary conditions, all faces except for face BFGC are prescribed the relevant symmetry conditions. We assign referential unit vectors $\mathbf{a}_0^{(1)}$ and $\mathbf{a}_0^{(2)}$ for two families of orthogonal collagen fibrils embedded in the sample as shown in Fig. 2. As an approximation, we let both families of collagen fibrils share a dispersion parameter of $\kappa = 0.1$.

*Simulation of photochemical reaction* The simulated distribution of riboflavin concentration captured at different times is shown in Fig. 3b, where it tends to reach a steady-state across the corneal thickness over time. On the other hand, as shown in Fig. 3c, the light intensity follows an exponential decay across the thickness, as is expected based

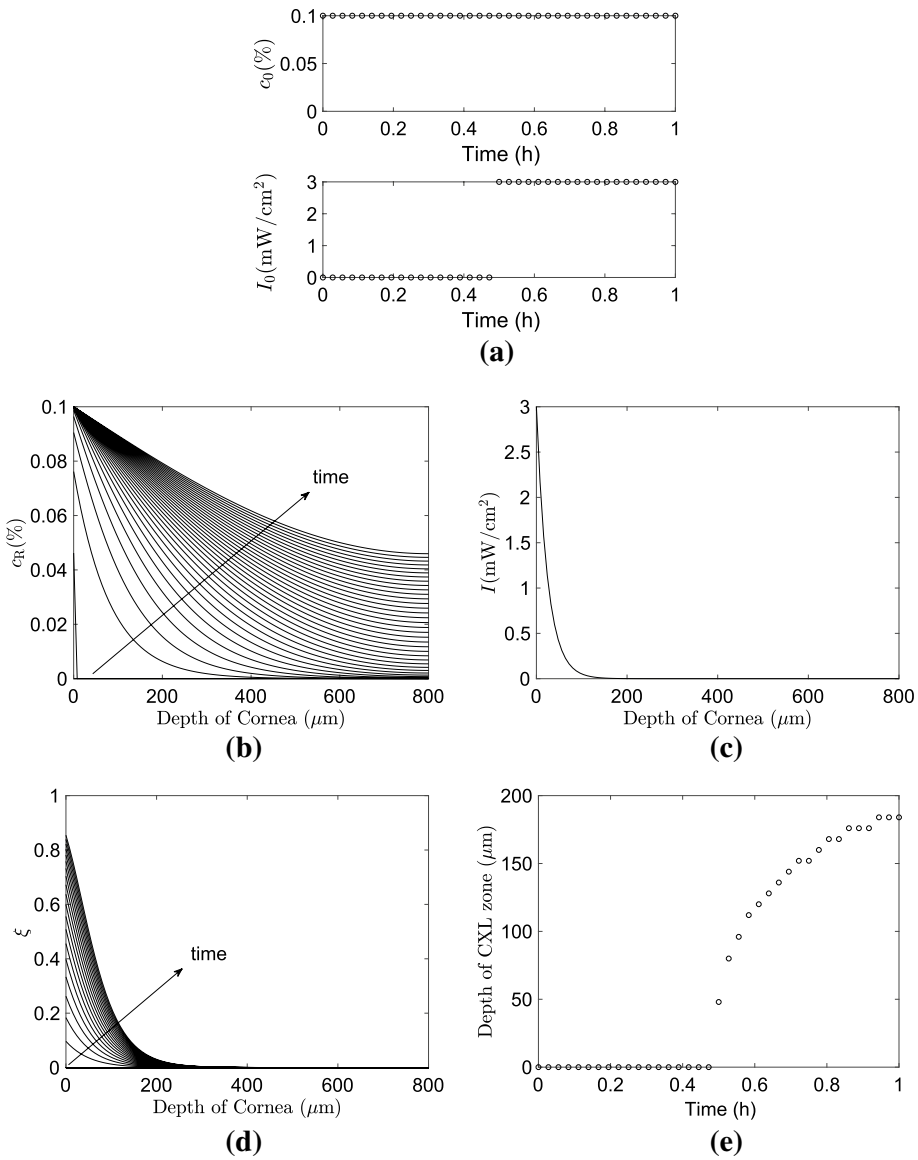


**Fig. 3** The simulation of photochemical reaction. **a** The prescribed riboflavin's concentration $c_0$ and light intensity $I_0$ as a function of time on face ABCD shown in Fig. 2, **b** the distribution of the riboflavin's concentration $c_R$ at different times, **c** the distribution of light intensity $I$ at the end of the simulation, **d** the distribution of degree of cross-linking $\xi$ at different times, and **e** the temporal evolution of effective cross-linking zone

on Eq. (2.4). We also see the photochemical reactions are much more pronounced at the anterior side, where both riboflavin and light intensity are at their highest level, as seen in Fig. 3d. Finally, we keep track of the depth of the effective cross-linking zone (the region where Young's modulus after the treatment reaches 140% of Young's modulus before the treatment) as a function of time; it shows that it increases rapidly once UV light is turned on and gradually reaches a steady-state over time, as shown in Fig. 3e.

*Genetic algorithm for parameter estimation* We calibrate our model to nanoindentation tests conducted by Seifert et al. (2014). Their experiments used eight pairs (16 total) of healthy porcine eyes; for each pair of eyes, one was exposed to UV irradiation, and the other serves as a control without UV exposure. The profiles of measured Young's modulus of eight UV treated samples are shown as circles, and the horizontal dashed lines represent Young's modulus of controls in each subfigure of Fig. 4. We employ a genetic algorithm in this work—an adaptive heuristic search algorithm capable of handling optimization problems with highly nonlinear and discontinuous objective functions. The genetic algorithm borrows the idea of natural selection that mimics gene evolution in biology, including inheritance, selection, crossover, and mutation (Wright 1991; Feng et al. 2017).

In practice, the genetic algorithm is used along with Python scripts to generate input files, execute jobs, and access the output database automatically in Abaqus. The genetic algorithm generates 50 genomes in every generation. For each genome, the corresponding Abaqus ".inp" file with the current set of material parameters is created. After running the simulation, the reaction force at the nine locations is obtained from the Abaqus output file. As required

**Table 1** Material parameters obtained from the literature

| Parameter | Value | Source |
|---|---|---|
| $D$ | $6.5 \times 10^{-7}\text{cm}^2/\text{s}$ | Kamaev et al. (2012) |
| $\epsilon_r$ | $235 \times\% \text{ cm}^{-1}$ | Kamaev et al. (2012) |
| $\sigma_c$ | $2.67 \text{ cm}^{-1}$ | Boettner and Dankovic (1974) |
| $\Phi$ | 0.38 | Islam et al. (2003) |

parameters is obtained when the objective function $f_{\text{obj}}$ is less than a tolerant of $\text{TOL} = 7.0 \times 10^{-7}$.

To further constrain our calibration, and preserve what is already known, some of our material parameters are taken directly from the existing literature. In particular, the diffusion coefficient of riboflavin $D = 6.5 \times 10^{-7}\text{cm}^2/\text{s}$ and the absorptivity of riboflavin $\epsilon_r = 235 \times\% \text{ cm}^{-1}$ (Kamaev et al. 2012), the absorptivity of cornea $\sigma_c = 2.67 \text{ cm}^{-1}$ (Boettner and Dankovic 1974), and the quantum yield $\Phi = 0.38$ (Islam et al. 2003). The parameters we have taken from the literature are summarized in Table 1. It is worth noting that the small deformation induced by the indentation barely produce limited information of the collagen fibrils' stretch locking behavior. Thus, the parameters $\{k_{20}, k_{21}\}$ are excluded in the calibration.

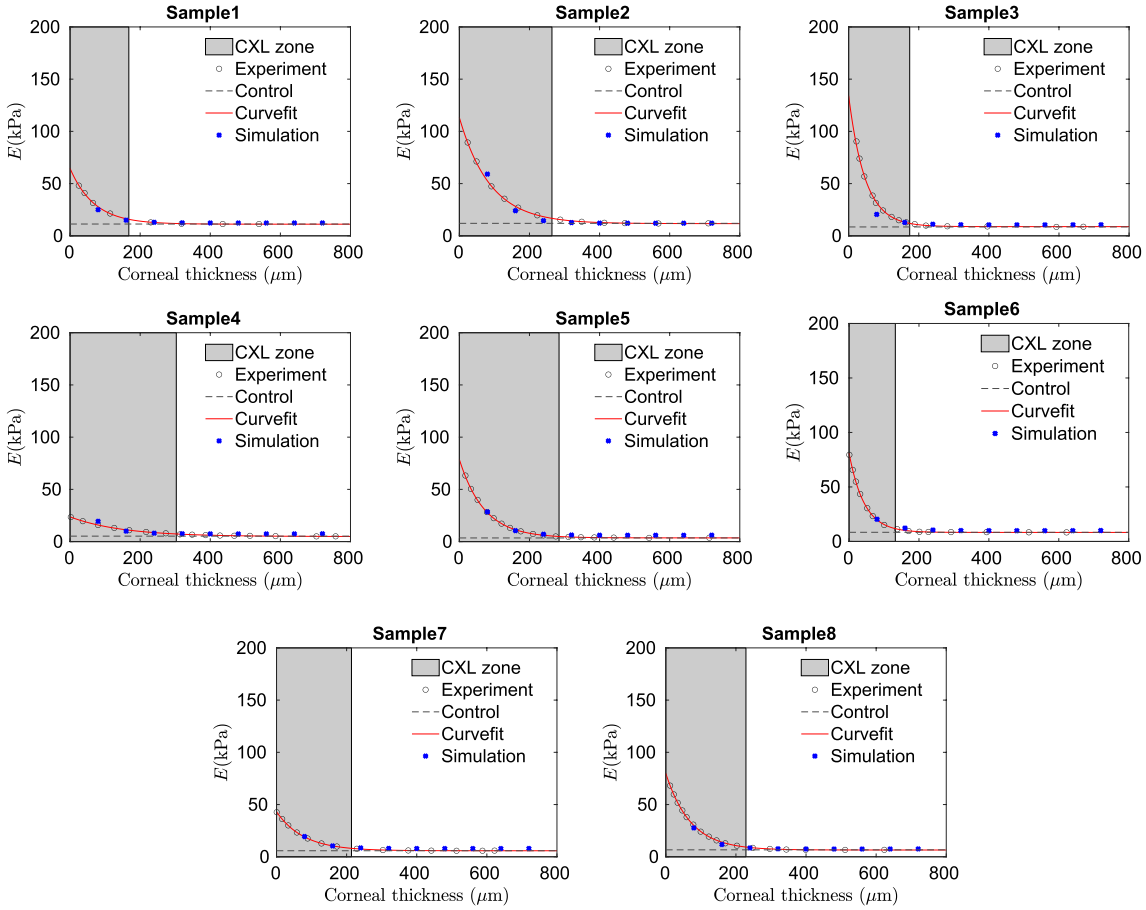


**Fig. 4** Comparison of Young's modulus $E$ corneal thickness curves between finite element simulations and experimental results of eight pairs of porcine eyes from Seifert et al. (2014). Here, the red curves denote the direct curve fitting to the experimental data, stars indicate our finite element simulations, and gray areas represent the effective cross-linked zones

by the genetic algorithm, we define an objective function as root-mean-squared-error of the indentation force between the simulation and experiment

$$f_{\text{obj}}(D, \epsilon_r, \ldots, k_{11}) = \sqrt{\frac{1}{n}\sum_{i=1}^{n}\left(F_i^{\text{sim}} - F_i^{\text{exp}}\right)^2}, \tag{3.1}$$

where $n$ is the total number of indentation data points in each simulation, $F_i^{\text{sim}}$ and $F_i^{\text{exp}}$ are simulated and experimentally measured reaction force at data point $i$. The optimal set of

Figure 4 shows our excellent model calibration to eight samples from Seifert et al. (2014), with the calibrated material parameters provided in Table 2.

**Table 2** Calibrated material parameters for the UV cross-linked samples based on data from Seifert et al. (2014)

| | Sample 1 | Sample 2 | Sample 3 | Sample 4 |
|---|---|---|---|---|
| $k_p$ (cm$^3$ mol$^{-1}$ s$^{-1}$) | 0.0028 | 0.0041 | 0.0039 | 0.0024 |
| $k_t$ (cm$^3$ mol$^{-1}$ s$^{-1}$) | 0.142 | 0.132 | 0.147 | 0.131 |
| $G_0$ (kPa) | 4.6 | 4 | 3.2 | 2 |
| $G_1$ (kPa) | 21.1 | 87.4 | 16.5 | 24 |
| $k_{10}$ (kPa) | 17 | 33.1 | 35.6 | 13.9 |
| $k_{11}$ (kPa) | 35.6 | 73 | 72.7 | 28.4 |
| | Sample 5 | Sample 6 | Sample 7 | Sample 8 |
| $k_p$ (cm$^3$ mol$^{-1}$ s$^{-1}$) | 0.0032 | 0.0035 | 0.0031 | 0.0035 |
| $k_t$ (cm$^3$ mol$^{-1}$ s$^{-1}$) | 0.153 | 0.166 | 0.127 | 0.134 |
| $G_0$ (kPa) | 1.3 | 3.2 | 2.4 | 1.6 |
| $G_1$ (kPa) | 42 | 20 | 22.9 | 34.3 |
| $k_{10}$ (kPa) | 9.6 | 20.2 | 11.4 | 46.8 |
| $k_{11}$ (kPa) | 77.5 | 102 | 25.9 | 56.1 |

Note that the red curves denote the direct curve fitting to the experimental data, stars indicate our finite element simulations, and gray areas represent the effective cross-linked zones.

### 3.2 Simulation of inflation tests from the literature

The results presented in this section are based on the experimental work of Kling et al. (2010) and consist of of (1) the intake of riboflavin for the first half-hour, (2) UV irradiation for another half hour, and (3) the mechanical inflation test on both control and UV cross-linked corneal samples.

*Corneal geometry* The corneal geometry of porcine is not explicitly specified in Kling et al. (2010). However, we could use the well-recorded human data because of their close similarity with porcine corneas in geometry and structure (Anderson et al. 2004; Pandolfi and Holzapfel 2008). To construct the corneal geometry, we adopt a generic biconic surface equation proposed by Pandolfi and Holzapfel (2008), which is based on the cylindrical coordinates $\{\Theta, r, x_3\}$, as seen in Fig. 5a. The equation for both anterior and posterior surfaces is given by

$$x_3 - \beta + \frac{r^2\gamma}{1+\sqrt{1-r^2\zeta}} = 0 \tag{3.2}$$

with

$$\gamma = \frac{\cos^2(\Theta-\Theta_{x_1})}{R_{x_1}} + \frac{\sin^2(\Theta-\Theta_{x_1})}{R_{x_2}} \tag{3.3}$$

and

$$\zeta = (Q_{x_1}+1)\frac{\cos^2(\Theta-\Theta_{x_1})}{R_{x_1}^2} + (Q_{x_2}+1)\frac{\sin^2(\Theta-\Theta_{x_1})}{R_{x_2}^2}. \tag{3.4}$$

Here, $\beta$ is the maximum vertical height at $r=0$, both $R_{x_1}$ and $R_{x_2}$ are the maximum curvatures of the principal meridians along $x_1$ and $x_2$ directions, respectively. $\Theta_{x_1}$ is the direction of the steepest principal meridian, both $Q_{x_1}$ and $Q_{x_2}$ are the asphericity parameters in the directions $\Theta_{x_1}$ and $\Theta_{x_1}+\pi/2$, respectively. The parameters used for our simulations are based on the average geometrical data over 114 subjects (Pandolfi and Holzapfel 2008). Specifically, for the posterior surface, the following geometrical parameters were used, $R_{x_1}=7.71$ mm, $R_{x_2}=7.87$ mm, $\Theta_{x_1}=0.51\pi$, $Q_{x_1}=Q_{x_2}=-0.41$, and $\beta=2.52$ mm. For the posterior surface, the following geometrical parameters were used, $R_{x_1}=6.36$ mm, $R_{x_2}=6.69$ mm, $\Theta_{x_1}=0.51\pi$, $Q_{x_1}=Q_{x_2}=-0.52$, and $\beta=1.89$ mm.

*Organization of collagen fibrils* Guided by the schematic shown in Fig. 1, we use referential unit vectors $\mathbf{a}_0^{(1)}$ and $\mathbf{a}_0^{(2)}$ to represent mean orientations of two families of collagen fibrils in cornea (Fig. 5b). In the central region, the collagen fibrils follow an orthogonal pattern. In the limbus region, one family of collagen fibrils runs circumferentially, while another runs radially.

For simplicity, we assume that both families of collagen fibrils share the same dispersion parameter $\kappa$. Prior work on the corneal structure via X-ray scattering showed that the dispersion of collagen fibrils is found to be varying spatially throughout the cornea (Aghamohammadzadeh et al. 2004). As a good approximation, we adopt the work from Pandolfi and Holzapfel (2008), in which the dispersion parameter $\kappa$ is assumed to be a periodic function of $\Theta$,

$$\kappa(\Theta) = \left(\frac{\kappa^{\min} + \kappa^{\max}}{2}\right) - \left(\frac{\kappa^{\max} - \kappa^{\min}}{2}\right)\cos 4\Theta. \quad (3.5)$$

The maximum and minimum values of dispersion parameter are taken to be $\kappa^{\max} = 0.333$ and $\kappa^{\max} = 0.133$, respectively. After adding the dependency of $r$, Eq. (3.5) finally becomes

$$\kappa(\Theta, r) = \kappa^{\min} + \frac{1}{2}\left(\kappa(\Theta) - \kappa^{\min}\right)\left(1 - \cos\frac{2\pi r}{R_{\mathrm{TZ}}}\right), \quad (3.6)$$

where $R_{\mathrm{TZ}} = 5.5$ mm denotes the radius of the transition zone. Note that we assign a homogeneous dispersion parameter of $\kappa = 0.3$ in the limbus region. Figure 5c visualizes the contour plot of dispersion parameter $\kappa$, as described by Eq. (3.6). It is clear that the collagen fibrils are more aligned with the two mean orientations (i.e., N-T and I-S directions), while more isotropically distributed at the optical center zone.

*Finite element mesh and boundary conditions* Our computational domain is partitioned into central and limbus regions, as shown in Fig. 5a. The entire domain is discretized into 3268 8-node brick elements with 6 elements spanning the thickness, and note that only a quarter of the entire corneal geometry is considered in our computation due to the symmetry. Similar to Sect. 3.1, we strictly follow the standard protocols, where the riboflavin with a concentration of $c_0 = 0.1\%$ and the UV light with an intensity of $I_0 = 3$ mW/cm$^2$ are prescribed at a circular shaded region with a radius of $r = 4$ mm, while the rest of the boundary is subjected to zero flux condition $\breve{j} = 0$. We also assume that the UV light propagates in $x_3$ direction ($\mathbf{d} = \mathbf{e}_3$). As for the mechanical boundary conditions, we fully fix the surface linking the limbus and sclera, the appropriate symmetry conditions are prescribed to all planes of symmetry. Additionally, for the inflation step, we gradually apply an internal pressure of $P = 50$ mmHg to the posterior surface following what was done in the experiments of Kling et al. (2010).

*Calibration to experimental data from the literature* Here, we compare our simulations against the experiments by Kling et al. (2010) to complete the calibration and emphasize our model's capability of capturing the overall biomechanical changes induced by the UV cross-linking. The material parameters are determined by calibrating our model to the intraocular pressure-apical displacement curves through a trial and error procedure. Since Kling et al. (2010) didn't specifically mention photochemical properties in their experiments, we use the previously calibrated photochemical parameters of sample 2 in Sect. 3.1 to reproduce a reasonable photochemical profile and restrict ourselves only on searching for the mechanical parameters of $\{G_0, G_1, k_{10}, k_{11}, k_{20}, k_{21}\}$. The calibration consists of two steps, first obtaining the initial parameters of $\{G_0, k_{10}, k_{20}\}$ by model calibration to control samples, followed by obtaining the fully cross-linked parameters of $\{G_1, k_{11}, k_{21}\}$ by model calibration to UV cross-linked samples while keeping the initial parameters fixed.

**Table 3** Calibrated mechanical parameters based on data from Kling et al. (2010)

| $G_0$ (kPa) | $G_1$ (kPa) | $k_{10}$ (kPa) | $k_{11}$ (kPa) | $k_{20}$ (–) | $k_{21}$ (–) |
|---|---|---|---|---|---|
| 3 | 120 | 40 | 200 | 100 | 3000 |

The simulated results at the last frame, regarding the photochemical reactions, are shown in Fig. 6a–c. In particular, Fig. 6a shows that the light intensity $I$ decays rapidly through the corneal thickness. The simulated contour of riboflavin's concentration $c_{\mathrm{R}}$ in Fig. 6b indicates that it penetrates more thoroughly at the central region than at the limbus region. We also find that with the previously measured diffusion coefficient, the riboflavin can not reach a homogeneous distribution across the corneal thickness by the end of the UV irradiation. Similar to the 1-D case, the degree of cross-linking $\xi$ is more pronounced at the anterior side, and it decays through the corneal thickness, as shown in Fig. 6c. More importantly, we report the biomechanical response of both control and UV cross-linked corneal samples. Figure 6d shows good agreement between simulations and experiments in terms of the intraocular pressure-apical displacement curves. The calibrated mechanical parameters used in the simulations are provided in Table 3. We also show the simulated effective stretch contour $\bar{\lambda} = \sqrt{\mathrm{tr}\mathbf{C}/3}$ of both control and UV cross-linked samples in Fig. 6e. As we expected, the UV cross-linked sample exhibits a smaller apical displacement than the control one under the same pressure loading. Interestingly, both samples share a "cross" pattern in the effective stretch contour—a lower value at the central region—induced by the collagen fibrils' stretching.

## 4 Concluding remarks

In conclusion, we have developed a multi-physics model and robust numerical simulation capability to model the UV cross-linking treatment for the cornea in full 3-D. Our model combines radiative transfer, migration of photo-initiator, photochemical reactions, and large deformation biomechanics. The novelty of this work lies in the robust finite element implementation of our multi-physics model, which may one day potentially allow medical professionals to do customizable surgical planning based on each patient's corneal geometry. Furthermore, model calibration is done by comparing our simulated results against a set of nanoindentation tests by Seifert et al. (2014) and inflation tests by Kling et al. (2010), respectively.

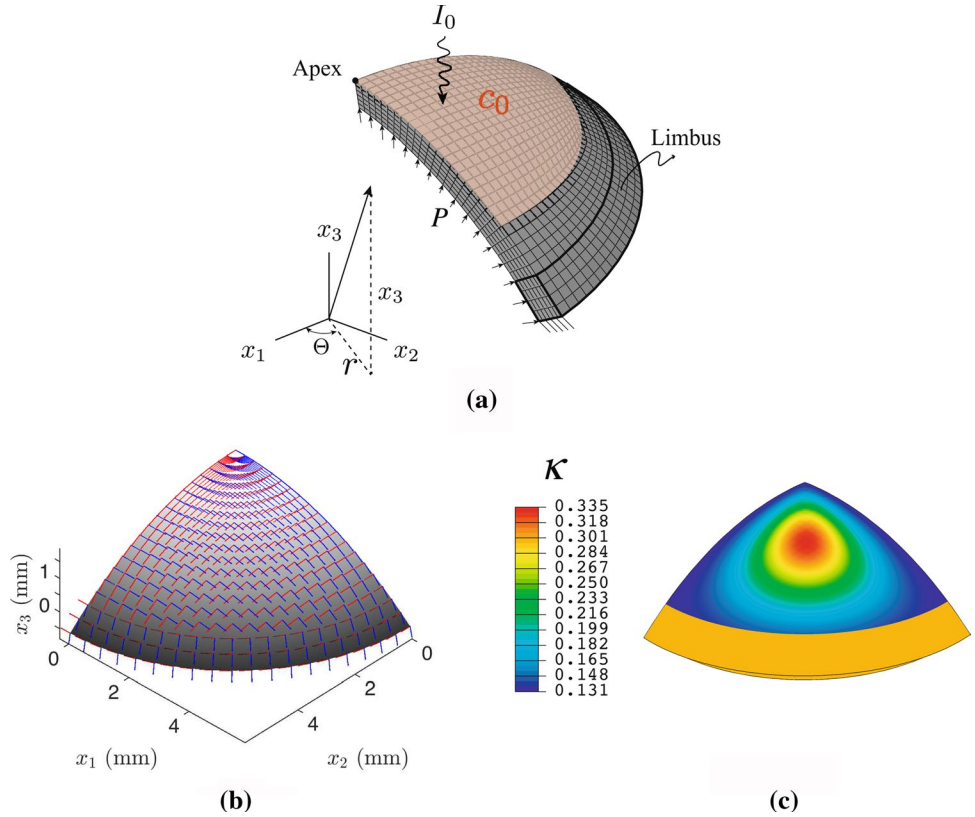


**Fig. 5** Geometry, organization of the collagen fibrils, and boundary conditions used in the inflation simulation. **a** The finite element mesh, along with the applied boundary conditions. **b** The main orientation of two families of collagen fibrils is represented as two unit vectors of $\mathbf{a}_0^{(1)}$ (red) and $\mathbf{a}_0^{(2)}$ (blue). **c** The spatial variation of dispersion parameter $\kappa$

Looking towards the future, the work yet remains. For example, oxygen plays an essential role in improving both efficiency and effectiveness of the treatment (Kamaev et al. 2012; Kling and Hafezi 2017); thus, the inclusion of oxygen and its diffusion may be considered in the future.

## Appendix 1: Finite element implementation

The weak forms of the coupled PDEs are discretized and approximated using linear elements, and the overall system is solved implicitly with a Newton method. Because of the well-known instability issue of the first order hyperbolic PDE governing the radiative transfer, we employ the streamline upwind Petrov-Galerkin formulation (SUPG) introduced by Brooks and Hughes (1982), where the weighting function takes the form

$$\bar{w}_1 = w_1 + \tau \mathbf{d} \cdot \mathrm{grad} w_1, \tag{4.1}$$

where $w_1$ is the standard weighting function, and $\tau$ is the SUPG stabilization parameter determined by the element size.[2] This gives the weighting function more influence in the upwind direction along the "streamline" which is $\mathbf{d}$. On the other hand, the weighting functions $w_2$ and $\mathbf{w}_3$ for the other PDEs follow the standard Galerkin method. The weak forms of Eqs. (2.21), (2.22), and (2.23) are based on the following weighted residuals

$$\left.\begin{aligned} &\int_{\mathcal{B}_t} \bar{w}_1 \Big( \mathbf{d} \cdot \mathrm{grad} I + \sigma I \Big) \mathrm{d}v = 0, \\ &\int_{\mathcal{B}_t} w_2 \Big( \dot{c}_\mathrm{R} - \mathrm{div}(D \mathrm{grad} c_\mathrm{R}) \Big) \mathrm{d}v = 0, \\ &\int_{\mathcal{B}_t} \mathbf{w}_3 \cdot \mathrm{div}\mathbf{T} \mathrm{d}v = \mathbf{0}. \end{aligned}\right\} \tag{4.2}$$

As is routine, the body is discretized into finite elements such that $\mathcal{B}_t = \cup \mathcal{B}_t^e$ and the nodal variables are taken to be the light intensity, concentration of riboflavin, and displacement, which are interpolated inside each element by

$$I = \sum I^A N^A, \quad c_\mathrm{R} = \sum c_\mathrm{R}^A N^A, \quad \text{and} \quad \mathbf{u} = \sum \mathbf{u}^A N^A \tag{4.3}$$

with the index $A = 1, 2, \ldots$ denoting the nodes of the element, $I^A$, $c_\mathrm{R}^A$, and $\mathbf{u}^A$ are the nodal UV light intensities, concentrations of riboflavin, and displacements, respectively, and $N^A$ the shape functions. Next, the weighting fields $w_2$

[2] Readers could refer to the work by Brooks and Hughes (1982) for more details.

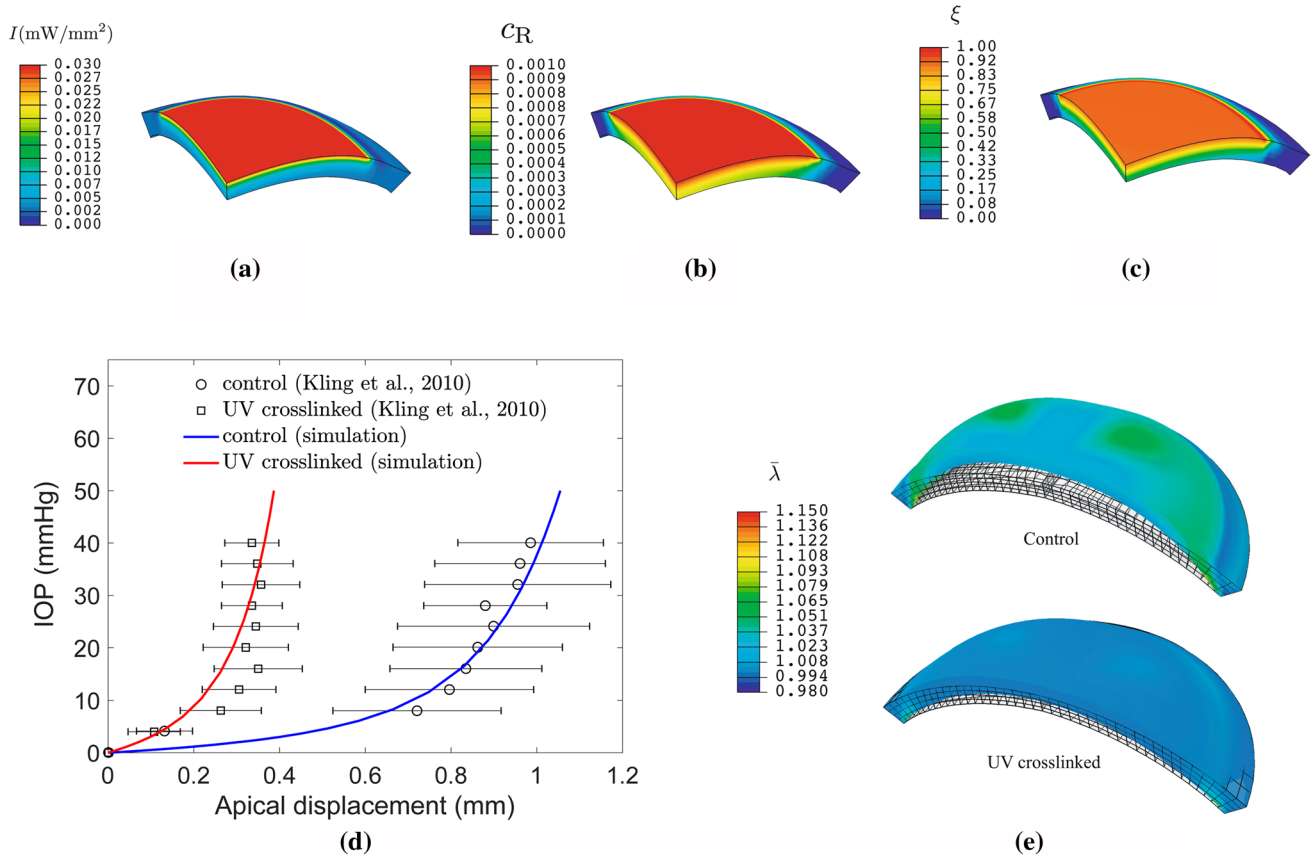


**Fig. 6** Simulated results of the inflation tests. For clarity, both quarter and half of the entire corneal geometry are shown here. Contour plots of **a** light intensity $I$, **b** the concentration of riboflavin $c_R$, and **c** the degree of cross-linking $\xi$. **d** The intraocular pressure-apical displacement curves. **e** The simulated contours of effective stretch $\bar{\lambda}$ of control and UV cross-linked corneal samples under an intraocular pressure of $P = 50$ mmHg; the referential mesh is superimposed for the comparison

and $\mathbf{w}_3$ are interpolated by the same shape functions in the Galerkin approach, while $\bar{w}_1$ uses the SUPG approach,

$$\begin{aligned} \bar{w}_1 &= \sum \left( w_1^A N^A + w_1^A \tau \mathbf{d} \cdot \mathrm{grad} N^A \right), \\ w_2 &= \sum w_2^A N^A, \quad \text{and} \quad \mathbf{w}_3 = \sum \mathbf{w}_3^A N^A. \end{aligned} \tag{4.4}$$

After substitution of Eqs. (4.3) and (4.4) into the weak forms, we arrive at the three element level of residuals. First, the element level residual for the UV light intensity $I(\mathbf{x}, t)$ is given by

$$\begin{aligned} R_I^A = & \underbrace{\int_{\mathcal{B}_t^e} N^A \left( \mathbf{d} \cdot \mathrm{grad} I + \sigma I \right) \mathrm{d}v}_{\text{Galerkin term}} \\ & + \underbrace{\int_{\mathcal{B}_t^e} \tau \left( \mathbf{d} \cdot \mathrm{grad} N^A \right) \left( \mathbf{d} \cdot \mathrm{grad} I + \sigma I \right) \mathrm{d}v}_{\text{Stabilization term}} . \end{aligned} \tag{4.5}$$

Second, the element level residual for the concentration of riboflavin $c_R(\mathbf{x}, t)$ is given by

$$R_c^A = \int_{\mathcal{B}_t^e} \left( N^A \dot{c}_{\mathrm{R}} \right) \mathrm{d}v + \int_{\mathcal{B}_t^e} \left( \mathrm{grad} N^A \right) D \left( \mathrm{grad} c_{\mathrm{R}} \right) \mathrm{d}v + \int_{\mathcal{S}_{\mathbf{j}}^e} \left( N^A \check{j} \right) \mathrm{d}a \,. \tag{4.6}$$

And the third element level residual for the displacement field $\mathbf{u}(\mathbf{x}, t)$ is given by

$$\mathbf{R}_{\mathbf{u}}^A = - \int_{\mathcal{B}_t^e} \mathbf{T} \, \mathrm{grad} N^A \mathrm{d}v + \int_{\mathcal{S}_{\mathbf{t}}^e} N^A \check{\mathbf{t}} \mathrm{d}a. \tag{4.7}$$

These three element level residuals are assembled into a global residual, which, when set to zero, represents a system of nonlinear equations for the nodal degrees of freedom.

The following tangents

$$(K_{cc})^{AB} = -\frac{\partial R_c^A}{\partial c_{\mathrm{R}}^B}, \quad (K_{cI})^{AB} = -\frac{\partial R_c^A}{\partial I^B}, \quad (\mathbf{K}_{c\mathbf{u}})^{AB} = -\frac{\partial R_c^A}{\partial \mathbf{u}^B},$$
$$(K_{Ic})^{AB} = -\frac{\partial R_I^A}{\partial c_{\mathrm{R}}^B}, \quad (K_{II})^{AB} = -\frac{\partial R_I^A}{\partial I^B}, \quad (\mathbf{K}_{I\mathbf{u}})^{AB} = -\frac{\partial R_I^A}{\partial \mathbf{u}^B},$$
$$(\mathbf{K}_{\mathbf{u}c})^{AB} = -\frac{\partial R_{\mathbf{u}}^A}{\partial c_{\mathrm{R}}^B}, \quad (\mathbf{K}_{\mathbf{u}I})^{AB} = -\frac{\partial R_{\mathbf{u}}^A}{\partial I^B}, \quad (\mathbf{K}_{\mathbf{uu}})^{AB} = -\frac{\partial R_{\mathbf{u}}^A}{\partial \mathbf{u}^B},$$

are required by the iterative Newton–Raphson procedure for convergence.

More specifically, the tangent $K_{cc}^{AB}$ is given by

$$K_{cc}^{AB} = - \int_{\mathcal{B}_t^e} N^A N^B \Delta t^{-1} \mathrm{d}v - \int_{\mathcal{B}_t^e} \frac{\partial N^A}{\partial x_i} D \frac{\partial N^B}{\partial x_i} \mathrm{d}v - \int_{\mathcal{S}_{\mathbf{j}}^e} N^A N^B \frac{\partial \check{j}}{\partial c} \mathrm{d}a. \tag{4.8}$$

The tangent $K_{II}^{AB}$ is given by

$$K_{II}^{AB} = - \int_{\mathcal{B}_t^e} N^A \left( d_i \frac{\partial N^B}{\partial x_i} + \epsilon_r \frac{\partial c_{\mathrm{R}}}{\partial I} I N^B + \sigma N^B \right) \mathrm{d}v - \int_{\mathcal{B}_t^e} \tau \left( d_i \frac{\partial N^A}{\partial x_i} \right) \left( d_i \frac{\partial N^B}{\partial x_i} + \sigma N^B + \epsilon_r \frac{\partial c_{\mathrm{R}}}{\partial I} I N^B \right) \mathrm{d}v. \tag{4.9}$$

The tangent $K_{cI}^{AB}$ is given by

$$K_{cI}^{AB} = - \int_{\mathcal{B}_t^e} N^A \frac{\partial \dot{c}_{\mathrm{R}}}{\partial I} N^B \mathrm{d}v - \int_{\mathcal{B}_t^e} \frac{\partial N^A}{\partial x_i} \frac{\partial D}{\partial I} \frac{\partial c_{\mathrm{R}}}{\partial x_i} N^B \mathrm{d}v. \tag{4.10}$$

The tangent $K_{Ic}^{AB}$ is given by

$$K_{Ic}^{AB} = - \int_{\mathcal{B}_t^e} N^A \epsilon_{\mathrm{r}} I N^B \mathrm{d}v - \int_{\mathcal{B}_t^e} N^A \left( \epsilon_{\mathrm{r}} c_{\mathrm{R}} + \sigma_c \right) \frac{\partial I}{\partial c_{\mathrm{R}}} N^B \mathrm{d}v - \int_{\mathcal{B}_t^e} \tau d_i \frac{\partial N^A}{\partial x_i} \epsilon_{\mathrm{r}} I N^B \mathrm{d}v - \int_{\mathcal{B}_t^e} \tau d_i \frac{\partial N^A}{\partial x_i} \frac{\partial I}{\partial c_{\mathrm{R}}} \left( \epsilon_{\mathrm{r}} c_{\mathrm{R}} + \sigma_c \right) N^B \mathrm{d}v. \tag{4.11}$$

The tangent $K_{\mathbf{uu}}^{AB}$ is given by

$$K_{u_i u_k}^{AB} = - \int_{\mathcal{B}_t^e} \frac{\partial N^A}{\partial x_j} \mathbb{A}_{ijkl} \frac{\partial N^B}{\partial x_l} \mathrm{d}v - \int_{\mathcal{S}_{\mathbf{t}}^e} N^A N^B \frac{\partial \check{t}_i}{\partial u_k} \mathrm{d}a, \tag{4.12}$$

where the spatial tangent modulus $\mathbb{A}$ is related to referential tangent modulus $\mathbb{A}_{\mathrm{R}}$ through

$$\mathbb{A}_{ijkl} = J^{-1} F_{jm} F_{ln} (\mathbb{A}_{\mathrm{R}})_{imkn}, \tag{4.13}$$

and the referential tangent modulus is given by $\mathbb{A}_{\mathrm{R}} \overset{\mathrm{def}}{=} \frac{\partial \mathbf{T}_{\mathrm{R}}}{\partial \mathbf{F}}$ with $\mathbf{T}_{\mathrm{R}} = J \mathbf{T} \mathbf{F}^{-\mathsf{T}}$ denoted as the Piola stress. We note that the coupling between deformation with other phenomenon is weak, thus we set $K_{c\mathbf{u}}^{AB}$, $K_{I\mathbf{u}}^{AB}$, $K_{\mathbf{u}c}^{AB}$, and $K_{\mathbf{u}I}^{AB}$ equal to zero as an approximation. Finally, to avoid volumetric-locking issues, we utilize the F-bar method of de Souza Neto et al. (1996) for fully-integrated elements. For complete details regarding the implementation of Abaqus user-element subroutines for multi-physics problems, readers are referred to Chester et al. (2015).

## Appendix 2: Verification of our finite element implementation

This section verifies our finite element implementations by comparing the numerical solutions with the analytically tractable solutions. Additionally, for non-tractable situations, numerical solutions are compared among themselves. Due to the complexity of the coupling, we consider it sufficient to verify each phenomenon separately.

First, we consider a simple and tractable situation for radiative transfer. We assume the extinction field $\sigma$ is homogeneous and independent of solvent concentration. The UV light propagates along the $x_1$ direction ($\mathbf{d} = \mathbf{e}_1$). Under these assumptions, the governing boundary value problem (2.21) is reduced to 1-D,

$$\begin{cases} \dfrac{dI}{dx_1} + \sigma I = 0 \quad \text{in} \quad 0 < x_1 \leq L, \\ I = I_0 \quad \text{on} \quad x_1 = 0. \end{cases} \tag{4.14}$$

The analytical solution is given by an exponential decay,

$$I(x_1) = I_0 \exp(-\sigma x_1). \tag{4.15}$$

The computational domain is a slender body with a length of $L = 0.4$ cm. We prescribe the UV light with an intensity of $I_0 = 3$ mW/cm$^2$ at $x_1 = 0$. For the purpose of a robust verification, we use three different homogeneous extinction fields of $\sigma = [10, 20, 100]$ cm$^{-1}$. We verify three types of elements: (1) 1-D linear element in Matlab, (2) 2-D four-node quadrilateral element in Abaqus, and (3) 3-D 8-node brick element in Abaqus. The comparisons are shown in Fig. 7a, where the analytical and numerical solutions are denoted as solid lines and markers, respectively. As we expected, our finite element implementations on the radiative transfer portion are verified.

Secondly, we move on to verify the pure diffusion problem. Similarly, the 1-D version of the diffusion equation (2.22) is given by

$$\begin{cases} \dot{c}_{\mathrm{R}} - D\dfrac{d^2 c_{\mathrm{R}}}{dx_1^2} = 0 \quad \text{in} \quad 0 < x_1 \le L, \\ \qquad c_{\mathrm{R}} = c_0 \quad \text{on} \quad x_1 = 0. \end{cases} \tag{4.16}$$

As an initial condition, we assume there is no riboflavin anywhere at $t = 0$. We prescribe the riboflavin with a concentration of $c_0 = 0.1\%$ at $x_1 = 0$. A diffusivity of $D = 6.5 \times 10^{-5}$ cm$^2$/s is used throughout the domain. The analytical solution is then given by

$$c = c_0 \mathrm{erfc}\left(\frac{x_1}{2\sqrt{Dt}}\right) \quad \text{with} \quad \mathrm{erfc}(\bullet) = \frac{2}{\pi}\int_{\bullet}^{\infty} \exp(-\tau^2)\mathrm{d}\tau. \tag{4.17}$$

Note that we use the same domain and mesh here. The verification taken at different times of $t = [10, 50, 100]$s in Fig. 7b shows excellent agreement between analytical and numerical solutions.

Next, we verify the photochemical reaction. The rate equation of monomer concentration was given by Eq. (2.13), and repeated here,

$$\begin{cases} -[\dot{M}] = k_{\mathrm{p}}[M]\sqrt{\dfrac{\Phi \epsilon_{\mathrm{r}} c_{\mathrm{R}} I}{k_{\mathrm{t}}}}, \\ [M](t=0) = [M_0]. \end{cases} \tag{4.18}$$

An initial monomer concentration of $[M_0] = 1000$ mol cm$^{-3}$ is given to close the problem. We take two rate constants and quantum yield to be $k_{\mathrm{p}} = 0.001$ cm$^3$ mol$^{-1}$ s$^{-1}$, $k_{\mathrm{t}} = 0.2$ cm$^3$ mol$^{-1}$ s$^{-1}$, and $\Phi = 0.38$, respectively. We consider a

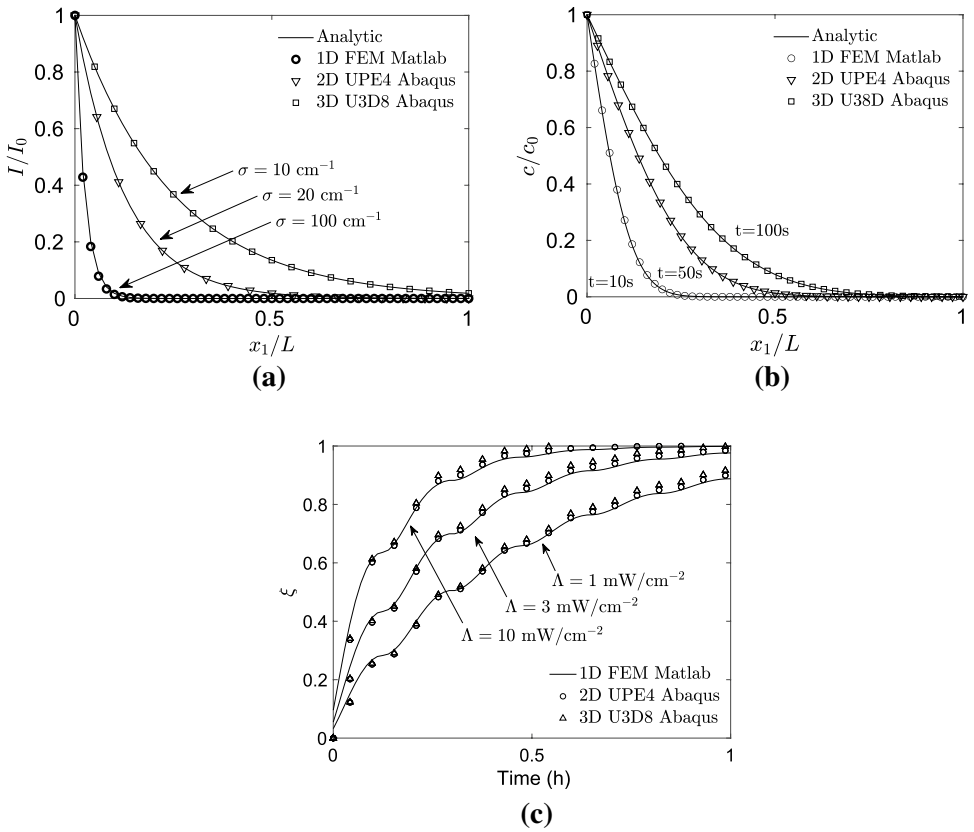


**Fig. 7** Code verification of **a** the radiative transfer problem with three different homogeneous light extension fields of $\sigma = [10, 20, 100]$ cm$^{-1}$, **b** the diffusion problem at $t = [10, 50, 100]$ s, and **c** the photochemical reaction problem with three different light magnitudes of $\Lambda = [1, 3, 10]$ mW/cm$^2$

homogeneous distribution of riboflavin with a concentration of $c_R = 0.1\%$. Additionally, we prescribe a homogeneous UV light with an fluctuating intensity of $I = \Lambda(1 + \sin \omega t)$ with a circular frequency of $\omega = 0.01$ rad/s and three different magnitudes of $\Lambda = [1, 3, 10]\,\mathrm{mW/cm^2}$ to ensure a robust verification. Unlike previous verifications, here, we use a single element and extract results from the integration point. Figure 7c shows a good agreement between programs on the evolution of the degree of cross-linking $\xi$.

Finally, we verify the pure mechanical problem. We prescribe a simple shear motion to a matrix cube embedded with a family of collagen fibrils with a referential orientation of $\mathbf{a}_0 = [1, 0, 0]^\mathrm{T}$ (Fig. 8a). As is well known, the corresponding deformation is given by (Gurtin et al. 2010)

$$[\mathbf{F}] = \begin{bmatrix} 1 & \gamma & 0 \\ 0 & 1 & 0 \\ 0 & 0 & 1 \end{bmatrix}, \quad [\mathbf{B}] = \begin{bmatrix} 1+\gamma^2 & \gamma & 0 \\ \gamma & 1 & 0 \\ 0 & 0 & 1 \end{bmatrix}, \quad [\mathbf{C}] = \begin{bmatrix} 1 & \gamma & 0 \\ \gamma & \gamma^2+1 & 0 \\ 0 & 0 & 1 \end{bmatrix} \tag{4.19}$$

with $\gamma = \tan\theta$ denotes the amount of shear. Based on Eq. (2.17), the analytical Cauchy stress is given by

$$\mathbf{T} = G\mathbf{B} + 2\left[k_1(I_\mathrm{f} - 1)\exp\left(k_2(I_\mathrm{f} - 1)^2\right)\right]\left[\mathbf{F}\mathbf{H}\mathbf{F}^\mathrm{T}\right] + P\mathbf{1}\,. \tag{4.20}$$

On the numerical side, a single 8-node brick element is prescribed with the same deformation. Figure 8b compares the analytical solutions for shear stress and normal stress difference given by

$$\begin{cases} T_{12} = G\gamma + 2\left[k_1(I_\mathrm{f} - 1)\exp\left(k_2(I_\mathrm{f} - 1)^2\right)\right]\left[\gamma\kappa\right] \\ T_{11} - T_{33} = G\gamma^2 + 2\left[k_1(I_\mathrm{f} - 1)\exp\left(k_2(I_\mathrm{f} - 1)^2\right)\right]\left[1 - 3\kappa + \gamma^2\kappa\right] \end{cases} \tag{4.21}$$

against the finite element solutions. Here, we use a dispersion parameter of $\kappa = 0.1$. Note that the stress is normalized by shear modulus $G$. The results show that the mechanical portion of our numerical implementation is verified.

## Appendix 3: Sensitivity study

We conduct a sensitivity study of our model by varying material parameters and boundary conditions used in the inflation simulation. Note that parameters and boundary conditions are varied one at a time by ±50% and ±100% around their calibrated values as used in Sect. 3.2, respectively.

We first vary the mechanical parameters for the control samples, $\{G_0, k_{10}, k_{20}\}$. Figure 9a–c show the corresponding variations in the simulated apical displacement-IOP curves along with the experimental data with arrows indicating the direction of increasing parameter value. The results suggest that $G_0$ and $k_{10}$ dictate the curve's initial slope, while $k_{20}$ determines the slope at the higher apical displacement for control samples.

Secondly, we vary parameters associated with the photochemical reaction, $\{D, \epsilon_\mathrm{r}, \Phi, k_\mathrm{p}, k_\mathrm{t}, \sigma_\mathrm{c}\}$. As arrows in Fig. 9d–i indicated, the overall stiffness increases with the increasing parameters except for the cases of $k_\mathrm{t}$ and $\sigma_\mathrm{c}$.

Next, we vary the mechanical parameters for the UV cross-linked samples, $\{G_1, k_{11}, k_{21}\}$. As expected, $G_1$ and $k_{11}$ control the initial stiffness, while $k_{21}$ controls the stretch-locking stiffness of the UV cross-linked samples (Fig. 9j–l).

Finally, we investigate the effect of the boundary conditions on the model's output by varying riboflavin's concentration $c_0$ and light intensity $I_0$ at the anterior surface. It is clear to us that both of them positively correlate with the

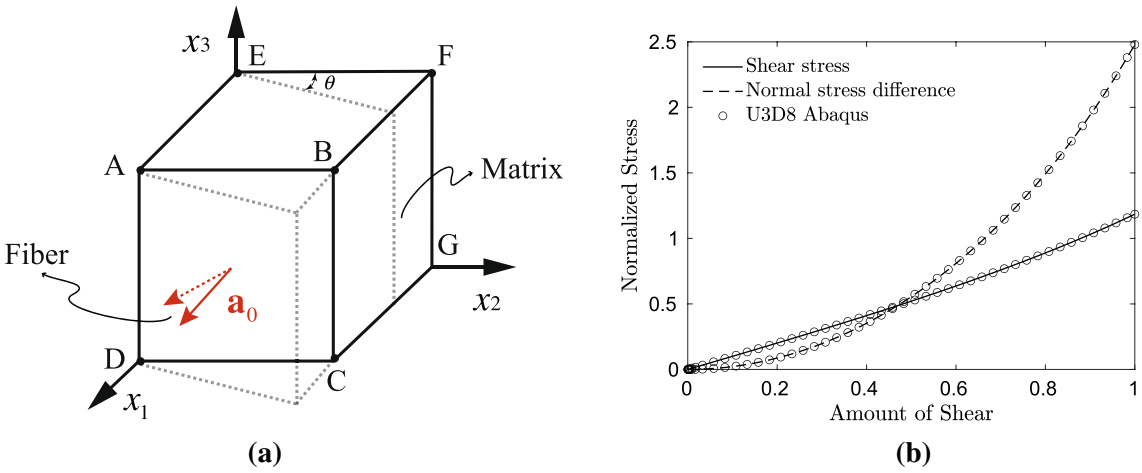


**Fig. 8** Code verification for the mechanical problem. **a** Schematic of a cubic cornea embedded with a single family of collagen fibrils with $\mathbf{a}_0 = [1, 0, 0]^\mathrm{T}$ denoted as the referential orientation. **b** The normalized shear stress $T_{12}/G$ and normalized normal stress difference $(T_{11} - T_{33})/G$ are plotted against the amount of shear $\gamma = \tan\theta$

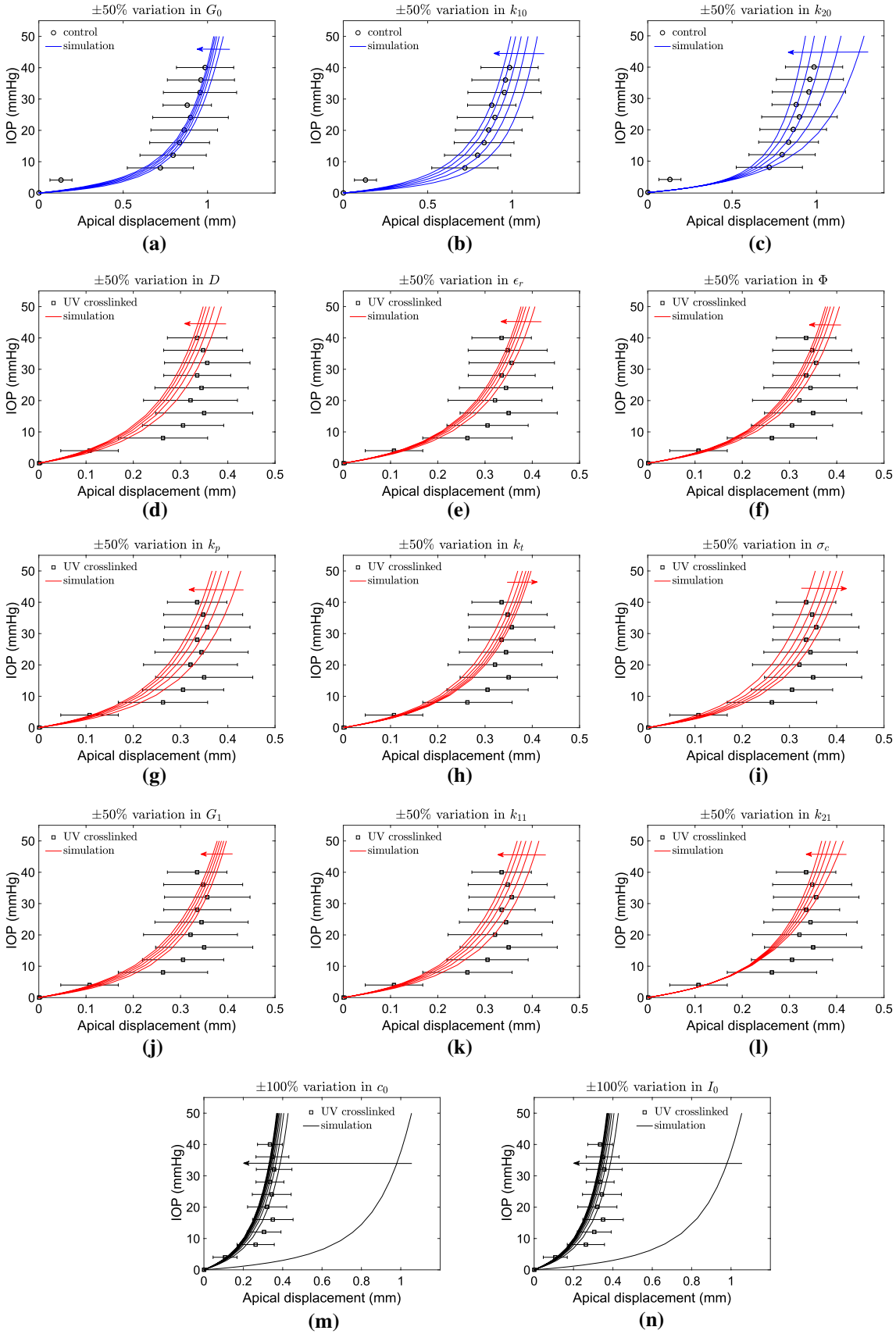


**Fig. 9** Sensitivity study of our model by varying material parameters and boundary conditions

overall stiffness of the UV cross-linked samples (Fig. 9m, n). More importantly, we note that the UV cross-linking process will eventually saturate as either $c_0$ or $I_0$ increases.

**Acknowledgements** SW thanks Maria A. Holland (University of Notre Dame) for many fruitful discussions and for the use of computational hardware and software. SAC acknowledges support from the National Science Foundation under Grant Number (CMMI-1751520).

## References

Abaqus/Standard. Abaqus Reference Manuals. Dassault Systemes Simulia, Providence, RI, 2019

Aghamohammadzadeh H, Newton RH, Meek KM (2004) X-ray scattering used to map the preferred collagen orientation in the human cornea and limbus. Structure 12(2):249–256

Ahmad I, Fasihullah Q, Noor A, Ansari IA, Ali QNM (2004) Photolysis of riboflavin in aqueous solution: a kinetic study. Int J Pharm 280(1–2):199–208

Anderson K, El-Sheikh A, Newson T (2004) Application of structural analysis to the mechanical behaviour of the cornea. J R Soc Interface 1(1):3–15

Beshtawi IM, Akhtar R, Hillarby MC, O'Donnell C, Zhao X, Brahma A, Carley F, Derby B, Radhakrishnan H (2013) Biomechanical properties of human corneas following low-and high-intensity collagen cross-linking determined with scanning acoustic microscopy. Investig Ophthalmol Vis Sci 54(8):5273–5280

Boettner EA, Dankovic D (1974) Ocular absorption of laser radiation for calculating personnel hazards. Technical report, Michigan Univ Ann Arbor School of Public Health

Bosnjak N, Wang S, Han D, Lee H, Chester SA (2019) Modeling of fiber-reinforced polymeric gels. Mech Res Commun 96:7–18

Brooks AN, Hughes TJ (1982) Streamline upwind/petrov-galerkin formulations for convection dominated flows with particular emphasis on the incompressible navier-stokes equations. Comput Methods Appl Mech Eng. 32(1–3):199–259

Caruso C, Epstein RL, Ostacolo C, Pacente L, Troisi S, Barbaro G (2017) Customized corneal cross-linking-a mathematical model. Cornea 36(5):600–604

Chandrasekhar S (2013) Radiative transfer. Courier Corporation

Chester SA, Leo CVD, Anand L (2015) A finite element implementation of a coupled diffusion-deformation theory for elastomeric gels. Int J Solids Struct 52:1–18

Dahl BJ, Spotts E, Truong JQ (2012) Corneal collagen cross-linking: an introduction and literature review. Optom J Am Optom Assoc 83(1):33–42

Dana MR, Putz JL, Viana MA, Sugar J, McMahon TT (1992) Contact lens failure in keratoconus management. Ophthalmology 99(8):1187–1192

de Souza Neto E, Perić D, Dutko M, Owen D (1996) Design of simple low order finite elements for large strain analysis of nearly incompressible solids. Int J Solids Struct 33(20–22):3277–3296

Feng Y, Lee C-H, Sun L, Ji S, Zhao X (2017) Characterizing white matter tissue in large strain via asymmetric indentation and inverse finite element modeling. J Mech Behav Biomed Mater 65:490–501

Gasser TC, Ogden RW, Holzapfel GA (2006) Hyperelastic modelling of arterial layers with distributed collagen fibre orientations. J R Soc Interface 3(6):15–35

Germann JA, Martínez-Enríquez E, Martínez-García MC, Kochevar IE, Marcos S (2020) Corneal collagen ordering after in vivo rose bengal and riboflavin cross-linking. Investig Ophthalmol Vis Sci 61(3):28

Goh K, Chen S, Liao K (2014) A thermomechanical framework for reconciling the effects of ultraviolet radiation exposure time and wavelength on connective tissue elasticity. Biomech Model Mechanobiol 13(5):1025–1040

Golomb G, Schoen FJ, Smith M, Linden J, Dixon M, Levy R (1987) The role of glutaraldehyde-induced cross-links in calcification of bovine pericardium used in cardiac valve bioprostheses. Am J Pathol 127(1):122

Goss B (2002) Bonding glass and other substrates with uv curing adhesives. Int J Adhesion Adhesives 22(5):405–408

Gurtin ME, Fried E, Anand L (2010) The mechanics and thermodynamics of continua. Cambridge University Press

Hamel CM, Cui F, Chester SA (2017) A finite element method for light activated shape-memory polymers. Int J Numer Methods Eng 111(5):447–473

Han D, Yang C, Fang NX, Lee H (2019) Rapid multi-material 3d printing with projection micro-stereolithography using dynamic fluidic control. Addit Manuf 27:606–615

Islam SD, Penzkofer A, Hegemann P (2003) Quantum yield of triplet formation of riboflavin in aqueous solution and of flavin mononucleotide bound to the lov1 domain of phot1 from chlamydomonas reinhardtii. Chem Phys 291(1):97–114

Jaeger MJ, Berson P, Kaufman H, Green W (1987) Epikeratoplasty for keratoconus: a clinicopathologic case report. Cornea 6(2):131–139

Kamaev P, Friedman MD, Sherr E, Muller D (2012) Photochemical kinetics of corneal cross-linking with riboflavin. Investig Ophthalmol Vis Sci 53(4):2360–2367

Kling S, Hafezi F (2017) An algorithm to predict the biomechanical stiffening effect in corneal cross-linking. J Refract Surg 33(2):128–136

Kling S, Remon L, Pérez-Escudero A, Merayo-Lloves J, Marcos S (2010) Corneal biomechanical changes after collagen cross-linking from porcine eye inflation experiments. Investig Ophthalmol Vis Sci 51(8):3961–3968

Kuo IC, Broman A, Pirouzmanesh A, Melia M (2006) Is there an association between diabetes and keratoconus? Ophthalmology 113(2):184–190

Lin J-T (2016) Combined analysis of safety and optimal efficacy in uv-light-activated corneal collagen crosslinking. Ophthalmol Res Int J:1–14

Lin J-T (2018) A critical review on the kinetics, efficacy, safety, nonlinear law and optimal protocols of corneal cross-linking. Of 10:35–38

Lovell LG, Lu H, Elliott JE, Stansbury JW, Bowman CN (2001) The effect of cure rate on the mechanical properties of dental resins. Dental Mater 17(6):504–511

Maruo S, Nakamura O, Kawata S (1997) Three-dimensional microfabrication with two-photon-absorbed photopolymerization. Opt Lett 22(2):132–134

Mazzotta C, Balestrazzi A, Traversi C, Baiocchi S, Caporossi T, Tommasi C, Caporossi A (2007) Treatment of progressive keratoconus by riboflavin-uva-induced cross-linking of corneal collagen: ultrastructural analysis by heidelberg retinal tomograph ii in vivo confocal microscopy in humans. Cornea 26(4):390–397

Odian G et al (2004) Principles of polymerization. John Wiley & Sons

Pandolfi A, Holzapfel GA (2008) Three-dimensional modeling and computational analysis of the human cornea considering distributed collagen fibril orientations. J Biomech Eng 130(6):061006

Petsche SJ, Pinsky PM (2013) The role of 3-d collagen organization in stromal elasticity: a model based on x-ray diffraction data and second harmonic-generated images. Biomech Model Mechanobiol 12(6):1101–1113

Rabinowitz YS (1998) Keratoconus. Surv Ophthalmol 42(4):297–319

Rad AS, Jabbarvand M, Saifi N (2004) Progressive keratectasia after laser in situ keratomileusis. J Refract Surg 20(5):S718–S722
Sadkowski A (2000) On the application of the logistic differential equation in electrochemical dynamics. J Electroanal Chem 486(1):92–94
Schumacher S, Oeftiger L, Mrochen M (2011) Equivalence of biomechanical changes induced by rapid and standard corneal cross-linking, using riboflavin and ultraviolet radiation. Investig Ophthalmol Vis Sci 52(12):9048–9052
Schumacher S, Mrochen M, Wernli J, Bueeler M, Seiler T (2012) Optimization model for uv-riboflavin corneal cross-linking. Investig Ophthalmol Vis Sci 53(2):762–769
Seifert J, Hammer CM, Rheinlaender J, Sel S, Scholz M, Paulsen F, Schäffer TE (2014) Distribution of young's modulus in porcine corneas after riboflavin/uva-induced collagen cross-linking as measured by atomic force microscopy. PLoS One 9(1):e88186
Seiler T, Huhle S, Spoerl E, Kunath H (2000) Manifest diabetes and keratoconus: a retrospective case-control study. Graefe's Arch Clin Exp Ophthalmol 238(10):822–825
Sekundo W, Stevens JD (2001) Surgical treatment of keratoconus at the turn of the 20th century. J Refract Surg 17(1):69–73
Semchishen A, Mrochen M, Semchishen V (2015) Model for optimization of the uv-a/riboflavin strengthening (cross-linking) of the cornea: percolation threshold. Photochem Photobiol 91(6):1403–1411
Singh M, Li J, Vantipalli S, Han Z, Larin KV, Twa MD (2017) Optical coherence elastography for evaluating customized riboflavin/uv-a corneal collagen crosslinking. J Biomed Opt 22(9):091504
Spoerl E, Huhle M, Seiler T (1998) Induction of cross-links in corneal tissue. Exp Eye Res 66(1):97–103
Spoerl E, Mrochen M, Sliney D, Trokel S, Seiler T (2007) Safety of uva-riboflavin cross-linking of the cornea. Cornea 26(4):385–389
Swinehart D (1962) The beer-lambert law. J Chem Edu 39(7):333
Wang S, Hatami-Marbini H (2021) Constitutive modeling of corneal tissue: influence of three-dimensional collagen fiber microstructure. J Biomech Eng 143(3):031002
Wang S, Decker M, Henann DL, Chester SA (2016) Modeling of dielectric viscoelastomers with application to electromechanical instabilities. J Mech Phys Solids 95:213–229
Watts DC (2005) Reaction kinetics and mechanics in photo-polymerised networks. Dental Mater 21(1):27–35
Wernli J, Schumacher S, Spoerl E, Mrochen M (2013) The efficacy of corneal cross-linking shows a sudden decrease with very high intensity uv light and short treatment time. Investig Ophthalmol Vis Sci 54(2):1176–1180
Wollensak G, Spoerl E, Seiler T (2003) Stress-strain measurements of human and porcine corneas after riboflavin-ultraviolet-a-induced cross-linking. J Cataract Refract Surg 29(9):1780–1785
Wright AH (1991) Genetic algorithms for real parameter optimization. Foundations of genetic algorithms, Elsevier 1:205–218